Radial Speed Evolution of Interplanetary Coronal Mass Ejections during Solar Cycle 23

T. Iju · M. Tokumaru · K. Fujiki

Solar-Terrestrial Environment Laboratory, Nagoya University, Furo-cho, Chikusa-ku, Nagoya, Aichi 464-8601, Japan

E-mail: tomoya@stelab.nagoya-u.ac.jp

Abstract We report radial-speed evolution of interplanetary coronal mass ejections (ICMEs) detected by *the Large Angle and Spectrometric Coronagraph* onboard *the Solar and Heliospheric Observatory* (SOHO/LASCO), interplanetary scintillation (IPS) at 327 MHz, and *in-situ* observations. We analyze solar-wind disturbance factor (*g*-value) data derived from IPS observations during 1997 – 2009 covering nearly the whole period of Solar Cycle 23. By comparing observations from SOHO/LASCO, IPS, and *in situ*, we identify 39 ICMEs that could be analyzed carefully. Here, we define two speeds [V_{SOHO} and V_{bg}], which are the initial speed of the ICME and the speed of the background solar wind, respectively. Examinations of these speeds yield the following results: i) Fast ICMEs (with $V_{SOHO} - V_{bg} > 500$ km s^{-1}) rapidly decelerate, moderate ICMEs (with 0 km s^{-1} $\leq V_{SOHO} - V_{bg} \leq 500$ km s^{-1}) show either gradually decelerating or uniform motion, and slow ICMEs (with $V_{SOHO} - V_{bg} < 0$ km s^{-1}) accelerate. The radial speeds converge on the speed of the background solar wind during their outward propagation. We subsequently find; ii) both the acceleration and the deceleration are nearly complete by 0.79 ± 0.04 AU, and those are ended when the ICMEs reach a 480 ± 21 km s^{-1}; iii) For ICMEs with ($V_{SOHO} - V_{bg}$) ≥ 0 km s^{-1}, *i.e.* fast and moderate ICMEs, a linear equation $a = -\gamma_1(V - V_{bg})$ with $\gamma_1 = 6.58 \pm 0.23 \times 10^{-6}$ s^{-1} is more appropriate than a quadratic equation $a = -\gamma_2(V - V_{bg})|V - V_{bg}|$ to describe their kinematics, where γ_1 and γ_2 are coefficients, and a and V are the acceleration and speed of ICMEs, respectively, because the χ^2 for the linear equation satisfies the statistical significance level of 0.05, while the quadratic one does not. These results support the assumption that the radial motion of ICMEs is governed by a drag force due to interaction with the background solar wind. These findings also suggest that ICMEs propagating faster than the background solar wind are controlled mainly by the hydrodynamic Stokes drag.

Keywords: *Coronal Mass Ejections, Initiation and Propagation; Coronal Mass Ejections, Interplanetary; Plasma Physics; Radio Scintillation.*

Abbreviations

ACE: *Advanced Composition Explorer*

AU: Astronomical unit

CC: Correlation coefficient

CDAW: Coordinated Data Analysis Workshop

CME: Coronal mass ejection

CPI: *Comprehensive Plasma Instrumentation*

ESA: European Space Agency

FOV: Field-of-view

GSFC: Goddard Space Flight Center

ICME: Interplanetary coronal mass ejection

IDED: IPS disturbance event day

IDEDs: IPS disturbance event days

IMP: *Interplanetary Monitoring Platform*

IPS: Interplanetary Scintillation

LASCO: *Large Angle and Spectrometric Coronagraph*

LOS: Line-of-sight

MIT: *Massachusetts Institute of Technology Faraday Cup Experiment*

NASA: National Aeronautics and Space Administration

OMNI: Operating Missions as Nodes on the Internet

SOHO: *Solar and Heliospheric Observatory*

STEL: Solar-Terrestrial Environment Laboratory

STEREO: *Solar-Terrestrial Relations Observatory*

SWE: *Solar Wind Experiment*

SWEPAM: *Solar Wind Electron, Proton, and Alpha Monitor*

1. Introduction

Coronal mass ejections (CMEs) are transient events in which large amounts of plasma are ejected from the solar corona (*e.g.* Gosling *et al.,* 1974). Interplanetary counterparts of CMEs are called interplanetary coronal mass ejections (ICMEs). Since ICMEs seriously affect the space environment around the Earth, understanding of their fundamental physics, *e.g.* generation, propagation, and interaction with the Earth's magnetosphere, is very important for space-weather forecasting (*e.g.* Tsurutani *et al.,* 1988; Gosling *et al.,* 1990). In particular, the dynamics of ICME propagation is one of the key pieces of information for predicting geomagnetic storms.

Propagation of ICMEs has been studied by various methods. Earlier studies combining space-borne coronagraphs with *in-situ* observations revealed that ICME speeds significantly evolve between near-Sun and 1 AU. Schwenn (1983) reported the correlation between CMEs and interplanetary disturbances using the *P78-1*/*Solwind* coronagraph, the *Helios-1* and -2 solar probes, and a ground-based Hα coronagraph. He showed that fast CMEs associated with flares exhibit no acceleration into interplanetary space, while slow CMEs related to prominence eruptions accelerate. Lindsay *et al.* (1999) examined the relation between propagation speeds of CMEs observed by the *Solwind* coronagraph and *Solar Maximum Mission* coronagraph/polarimeter and those of the ICMEs observed by the *Helios-1* and *Pioneer Venus Orbiter* for 31 CMEs and their associated ICMEs. They found a good correlation between the speeds of CMEs and those of ICMEs observed in interplanetary space between 0.7 and 1 AU. They also found that the speeds of most ICMEs range from 380 km s^{-1} to 600 km s^{-1}, while CME speeds show a wider range of from ≈10 km s^{-1} to 1500 km s^{-1}. These findings suggest that the ICME speeds tend to converge to an average solar-wind speed as they propagate through interplanetary space. Gopalswamy *et al.* (2000) determined an effective acceleration for 28 CMEs observed by the *Large Angle and Spectrometric Coronagraph* (LASCO: Brueckner *et al.,* 1995) onboard the *Solar and Heliospheric Observatory* (SOHO) spacecraft between 1996 and 1998. On the assumption that the acceleration is constant, they found a very good anti-correlation between the accelerations and initial speeds of CMEs, and a critical speed of 405 km s^{-1}; this value is close to the typical speed of the solar wind in the equatorial plane. Following this research, Gopalswamy *et al.* (2001) described an empirical model for predicting of arrival of the ICMEs at 1 AU; this model is based on their previous work (Gopalswamy *et al.,* 2000) and its accuracy is improved by allowing for cessation of the interplanetary acceleration before 1 AU. They showed that the acceleration cessation distance is 0.76 AU, and this result agrees reasonably well with observations by SOHO, *Advanced Composition Explorer* (ACE: Stone *et al.,* 1998), and other spacecraft at 1 AU.

We expect that the acceleration or deceleration of ICMEs is controlled by a drag force caused by interaction between ICMEs and the solar wind. Vršnak and Gopalswamy (2002) proposed an advanced model for the motion of ICMEs; this model considered the interaction with solar wind using a simple expression for the acceleration: $a = -\gamma_1(V - V_{bg})$, where γ_1, V, and V_{bg} are the coefficient, ICME speed, and speed of the background solar wind, respectively. They also compared their model with a drag-acceleration model $a = -\gamma_2(V - V_{bg})|V - V_{bg}|$, where γ_2 is the coefficient for this equation; this expression is known as the aerodynamic drag force (*e.g.* Chen, 1996; Cargill, 2004). Both models have been tested by comparing with CME observations. Tappin (2006) studied the propagation of a CME that occurred on 5 April 2003 using observations by the SOHO/LASCO, the *Solar Mass Ejection Imager* onboard the *Coriolis* satellite, and the *Ulysses* spacecraft. Maloney and Gallagher (2010) derived the three-dimensional kinematics for three ICMEs detected between 2008 and 2009 using the *Solar-Terrestrial Relations Observatory-A* (STEREO-A) and -B spacecraft observations. Temmer *et al.* (2011) examined the influence of the solar wind on the propagation of some ICMEs using the STEREO-A and -B spacecraft.

Although the propagation of ICMEs has been studied by many investigators, their dynamics is still not well understood. This is mainly due to the lack of observational data about ICMEs between 0.1 and 1 AU. Almost all ICME observations are currently limited to the near-Earth area in the equatorial plane.

Remote sensing using radio waves is a suitable method for collecting global data on ICMEs. For example, Reiner, Kaiser, and Bougeret (2007) derived kinematical parameters for 42 ICME/shocks from measurements of type-II radio emission. Woo (1988) studied the shock propagation using Doppler-scintillation measurements of radio waves emitted from planetary spacecraft, and showed the speed profiles of shocks between 0.05 and 0.93 AU. In addition to these measurements, interplanetary scintillation (IPS) is a type of remote sensing. IPS is a phenomenon where signals from a point-like radio source, such as quasars and active galactic nuclei, fluctuate due to density irregularities in the solar wind (Hewish, Scott, and Wills, 1964). IPS observations allow us to probe the inner heliosphere using many radio sources, and is a useful means to study the global structure and propagation dynamics of ICMEs in the solar wind (*e.g.* Gapper *et al.*, 1982; Tappin, Hewish, and Gapper, 1983; Watanabe and Kakinuma, 1986; Tokumaru *et al.*, 2000a; Manoharan *et al.*, 2000; Jackson and Hick, 2002; Tokumaru *et al.*, 2003; Bisi *et al.*, 2010; Jackson *et al.*, 2010; Manoharan, 2010; see also Watanabe and Schwenn, 1989). For the kinematics of interplanetary disturbances, Vlasov (1992) reported that the radial dependence of speed can be represented by a power-law function [$V \approx R^{-\alpha}$] with α in the range $0.25 < \alpha < 1$ from analysis of all-sky scintillation indices maps. Manoharan (2006) examined radial evolution of 30 CMEs observed by SOHO/LASCO, ACE, and the Ooty radio-telescope between 1998 and 2004. He showed that most CMEs tend to attain the speed of the ambient flow at 1 AU and also reported a power-law form of radial-speed evolution for these events.

We take advantage of IPS observation to determine the ICME speed and acceleration. In the current study, we analyze the solar-wind disturbance factor (*g*-value) derived from IPS observations during 1997 – 2009 covering nearly the whole of Solar Cycle 23 and make a list of disturbance event days in the period. We define an "ICME" as a series of events including a near-Sun CME, an interplanetary disturbance, and a near-Earth ICME in this study. By comparing our list with that of CME/ICME pairs, we identify many events that are detected at three locations between the Sun and the Earth's orbit, *i.e.* near-Sun, interplanetary space, and near-Earth, and derive their radial speed profiles. We then analyze the relationship between the acceleration and speed difference for the ICMEs. The outline of this article is as follows: Section 2 describes the IPS observations made with the 327 MHz radio-telescope system of the Solar-Terrestrial Environment Laboratory (STEL), Nagoya University. Section 3 describes the criteria for ICME identification and the method for estimating ICME speeds and accelerations between the corona and 1 AU. Section 4 provides the radial-speed profiles of ICMEs and the analyses of the propagation properties. Section 5 discusses the results, while Section 6 summarizes the main conclusions of our study.

2. STEL IPS Observations

STEL IPS observations have been carried out regularly since the early 1980s using multiple ground-based radio-telescope stations operated at 327 MHz (Kojima and Kakinuma, 1990; Asai *et al.*, 1995). The IPS observations at 327 MHz allow us to determine the solar-wind condition between 0.2 and 1 AU with a cadence of 24 hours. In our observations, nearly 30 radio sources within a solar elongation of 60° are observed daily between April and December. The IPS observations on a given day are made when each radio source traverses the local meridian.

The solar-wind speed and disturbance factor, the so called "*g*-value" (Gapper *et al.*, 1982), are derived from IPS observations. A *g*-value is calculated for each source using the following equation:

$$g = \frac{\Delta S}{\Delta S_{\mathrm{m}}(\varepsilon)} \ , \tag{1}$$

where ΔS and $\Delta S_{\mathrm{m}}(\varepsilon)$ are the observed fluctuation level of radio signals and their yearly mean, respectively. $\Delta S_{\mathrm{m}}(\varepsilon)$ varies with the solar elongation angle [ε] for a line-of-sight (LOS) from an observed radio source to a telescope. When a radio signal is weakly scattered, the *g*-value is given by the following equation (Tokumaru *et al.*, 2003; Tokumaru *et al.*, 2006):

$$g^2 = \frac{1}{K}\int_0^{\infty} \mathrm{d}\, z\{\Delta N\mathrm{e}\}^2\, w(z) \ , \tag{2}$$

here, z is the distance along a LOS, ΔNe is the fluctuation level of solar-wind (electron) density, K is the normalization factor based on the mean density fluctuation of the background solar wind, and $w(z)$ is the IPS weighting function (Young, 1971). We note that ΔNe is nearly proportional to the solar-wind density [*Ne*]; $\Delta N\mathrm{e} \propto N\mathrm{e}$ (Coles *et al.*, 1978), and the weak-scattering condition holds for $R > 0.2$ AU, where R is the radial distance from the Sun.

A *g*-value represents the relative level of density fluctuation integrated along a LOS. For quiet solar-wind conditions, the *g*-value is around unity. With dense plasma or high turbulence as an ICME passes across a LOS, the *g*-value becomes greater than unity because of the ΔNe ($\propto N$e) increase. In contrast, a *g*-value less than unity indicates a rarefaction of the solar wind. Hence, detecting an abrupt increase in *g*-value is a useful means to detect an ICME.

The location of the LOS for a radio source exhibiting a *g*-value enhancement in the sky plane indicates a turbulent region is present. A sky-map of enhanced *g*-values for the sources observed in a day is called a "*g*-map" (Gapper *et al.*, 1982; Hewish and Bravo, 1986). This map provides information on the spatial distribution of ICMEs. Figure 1 shows an example of a *g*-map for a CME event. A white-light difference image of a CME observed by the SOHO/LASCO-C2 coronagraph is shown in the left-hand panel of Figure 1. As shown here, a bright balloon-like structure was observed on the northeast limb on 11 July 2000. This event was reported as an asymmetric halo CME in the SOHO/LASCO CME Catalog (Yashiro *et al.*, 2004; Gopalswamy *et al.*, 2009; available at http://cdaw.gsfc.nasa.gov/CME_list/). The right-hand panel of Figure 1 is a *g*-map derived from our IPS observation on 12 July 2000. The center of the map corresponds to the location of the Sun, and the horizontal and vertical axes are parallel to the East–West and North–South directions, respectively. The concentric circles indicate the radial distances to the closest approach of the LOS of 0.3 AU, 0.6 AU, and 0.9 AU. The radial distance [r_{IPS}] for each LOS is given by $r_{\mathrm{IPS}} = r_{\mathrm{E}} \sin\varepsilon$, where r_{E} is the distance between the Sun and the Earth, *i.e.* 1 AU and ε is the solar elongation angle for the LOS. This calculation is based on the approximation that a large fraction of IPS is given by the wave scattering at the closest point to the Sun (the P-point) on a LOS (Hewish, Scott, and Wills, 1964). Since ten LOSs between 0.4 and 0.7 AU in the eastern hemisphere (left-hand side of *g*-map) exhibit high *g*-values, a group of them is considered as the interplanetary counterpart of the 11 July 2000 CME event. This CME was also detected by *in-situ* observation at 1 AU on 13 July 2000 and reported as a near-Earth ICME (Richardson and Cane, 2010).

In this way, a *g*-map can visualize an ICME between 0.2 and 1 AU. The *g*-value data have been available from our IPS observation since 1997 (Tokumaru *et al.*, 2000b). To find the *g*-value enhancements due to ICMEs from the *g*-value data obtained between 1997 and 2009, we define criteria for the ICME identifications as mentioned in the next section.

3. Method

3.1. ICME Identification

First, we define disturbance days due to an ICME in the IPS data. In this determination, we consider a threshold *g*-value and the number of sources exhibiting the threshold or beyond. The average [a_g] and standard deviation [σ_g] for the *g*-values obtained by STEL IPS observations between 1997 and 2009 are 1.07 and 0.47, respectively. From these, we regard a *g*-value for a disturbed condition on a given day to be $a_g + \sigma_g$ or more, and we decide to use 1.5 as this threshold. We also define an "observation day" as a day on which 15 or more sources are observed by our radio-telescope system; this minimum number is equal to half the mean number of sources observed in a day. In an observation day, when five or more sources showed a disturbed condition, we judge that a disturbance had occurred. Combining the above criteria, we define an "IPS disturbance event day" (IDED) as a day on which $g \geq 1.5$ sources numbered five or more on an observation day. Using this definition, we find 656 IDEDs in our period of research. From these, we eliminate periods with four or more consecutive IDEDs because they are likely related to co-rotating stream interaction regions (Gapper *et al.*, 1982). However, we do not eliminate two periods including the 2000 Bastille Day (illustrated in Figure 1) and 2003 Halloween events from among the IDEDs above because consecutive disturbances in them are caused by successive CMEs (*e.g.* Andrews, 2001; Gopalswamy *et al.*, 2005). As a result, 159 out of 656 IDEDs are excluded, and the remaining 497 IDEDs are listed as candidates for ICME events.

Next, we examine the relationship between CME/ICME pairs and selected IDEDs. In this examination, we use the list of near-Earth ICMEs and associated CMEs compiled by Richardson and Cane (2010). This includes 322 ICMEs associated with a halo or a partial halo or normal CMEs during Solar Cycle 23; here, "normal" means that the exterior of CME is neither a halo nor a partial halo. In the above study, CMEs were observed by the SOHO/LASCO coronagraphs, and ICMEs were detected by *in-situ* observation using spacecraft such as ACE and the *Interplanetary Monitoring Platform-8* (IMP-8). We compare the list of IDEDs with that of ICMEs using assumption that an ICME caused the IDED. When an IDED is between the appearance date of the associated CME and the detection date of a near-Earth ICME, we assume that the IDED was related to the ICME.

Using the above method, we find 66 IDEDs from our list that were probably related to ICMEs. However, we also find that 16 IDEDs of the 66 had multiple associated CMEs. For these 16 events, we identify the optimal one-to-one correspondence by comparing positions for LOS exhibiting high *g*-values in a *g*-map with the direction of the associated CME eruption in the LASCO field-of-view (FOV).

At the end of this selection, we identify 50 CMEs and their associated ICMEs that were detected by the SOHO/LASCO, IPS, and *in-situ* observations. For these, we estimate radial speeds and accelerations in interplanetary space using the method described in the next subsection.

3.2. Estimations of ICME Radial Speeds and Accelerations

The ICME radial speeds and accelerations are estimated in two interplanetary regions, *i.e.* the region between SOHO and IPS observations (the SOHO–IPS region, from 0.1 to ≈0.6 AU) and that between IPS and *in-situ* observations (the IPS–Earth region, from ≈0.6 to 1 AU). In these estimations, we assume that locations of LOS for disturbed sources in a *g*-map give the location of the ICME.

First, we calculate radial speeds at reference distances for each ICME. For each radio source of $g \geq 1.5$ in a *g*-map, distances [r_1 and r_2] and radial speeds [v_1 and v_2] are derived from the following equations:

$$r_1 = \frac{r_S + r_{IPS}}{2}, \quad v_1 = \frac{r_{IPS} - r_S}{t_{IPS} - T_{SOHO}} \qquad \text{(for the SOHO–IPS region)}, \quad (3)$$

and

$$r_2 = \frac{r_{\rm IPS} + r_{\rm E}}{2}, \quad v_2 = \frac{r_{\rm E} - r_{\rm IPS}}{T_{\rm Earth} - t_{\rm IPS}} \qquad \text{(for the IPS–Earth region),} \quad (4)$$

respectively. Here, $r_{\rm S}$ is the minimum radius of the SOHO/LASCO-C2 FOV, *i.e.* 0.009 AU, $r_{\rm IPS}$ is the radial distance of P-point on the LOS, $r_{\rm E}$ is the distance between the Sun and the Earth, *i.e.* 1 AU, $T_{\rm SOHO}$ is the appearance time of CME in SOHO/LASCO-C2 FOV, $t_{\rm IPS}$ is the observation time for a $g \geq 1.5$ source, and $T_{\rm Earth}$ is the onset time of near-Earth ICME by *in-situ* observation. Using these values, the average reference distances [R_1 and R_2] and the average radial speeds [V_1 and V_2] for the ICME are found for values of r_1, r_2, v_1, and v_2 for all $g \geq 1.5$ sources, respectively on a given day.

Next, we calculate accelerations using the values above. In these calculations, we use the approximation that the accelerations are constant within each region. The average accelerations, *i.e.* a_1 and a_2, for ICMEs were given by

$$a_1 = \frac{1}{n}\sum_{\rm k=1}^{\rm n} \frac{v_{\rm IPS,k} - V_{\rm SOHO}}{t_{\rm IPS,k} - T_{\rm SOHO}} \qquad \text{(for the SOHO–IPS region),} \quad (5)$$

and

$$a_2 = \frac{1}{n}\sum_{\rm k=1}^{\rm n} \frac{V_{\rm Earth} - v_{\rm IPS,k}}{T_{\rm Earth} - t_{\rm IPS,k}} \qquad \text{(for the IPS–Earth region),} \quad (6)$$

respectively. Here,

$$v_{\rm IPS,k} = \frac{v_{1,\rm k} + v_{2,\rm k}}{2} \quad , \qquad (7)$$

$t_{\rm IPS,k}$ is the observation time for each $g \geq 1.5$ source, n is the number of $g \geq 1.5$ sources, and $V_{\rm SOHO}$ and $V_{\rm Earth}$ are the radial speed of the CME and of the near-Earth ICME, respectively. For the value of $V_{\rm SOHO}$ in the halo or the partial halo CMEs, we use

$$V_{\rm SOHO} = 1.20 \times V_{\rm POS} \ , \qquad (8)$$

where $V_{\rm POS}$ is the speed measured in the sky plane by the SOHO/LASCO, because the coronagraph measurement for them tends to underestimate the radial speed (Michalek, Gopalswamy, and Yashiro, 2003), while we use $V_{\rm SOHO} = V_{\rm POS}$ for the normal ones. In this study, we use the linear speeds reported in the SOHO/LASCO CME Catalog (http://cdaw.gsfc.nasa.gov/CME_list/index.html) for those of $V_{\rm POS}$ with a 0.08 AU reference distance corresponding to half the LASCO FOV value. Those are derived from the bright leading edges of CME (Yashiro *et al.*, 2004), while the associated shocks show a faint structure ahead of them (Ontiveros and Vourlidas, 2009), and then indicate the speeds of CME itself in the sky plane (Vourlidas *et al.*, 2012). For values of $V_{\rm Earth}$, we use the average ICME speeds listed by Richardson and Cane (2010). We note that the values of $V_{\rm SOHO}$ and $V_{\rm Earth}$ represent an average in the near-Sun and near-Earth regions, respectively, and V_1, V_2, a_1, and a_2 are averages in the interplanetary space. The ICME speeds in the near-Earth region are measured when the spacecraft passes through them. Thus, those are equivalent to the plasma flow speed on the trajectory of the spacecraft during the passage of an ICME indicated by the enhancement of the charge state and the rotation of magnetic-field direction (Richardson and Cane, 2010). The speed of the solar wind measured by *in-situ* observations is sometimes highly variable during the passage of an ICME. However, the majority of ICMEs listed by them have only < 100 km s^{-1} difference between the peak and average speeds. Hence, we consider it justified that the average flow speed can be used as the propagation speed of ICMEs.

3.3. Classification of ICMEs

Here, we introduce $V_{\rm IPS}$ which is given as the average value of $v_{\rm IPS}$ for each ICME; the $v_{\rm IPS}$ is derived from Equation (7). In addition, we also introduce $V_{\rm bg}$ as the speed of the background solar wind. To determine the value of $V_{\rm bg}$ as the average background wind speed between

T_{SOHO} and T_{Earth} for each ICME, we used plasma data obtained by space-borne instruments including *Solar Wind Electron, Proton, and Alpha Monitor* onboard ACE (ACE/SWEPAM: McComas *et al.*, 1998), *Solar Wind Experiment* on *Wind* (*Wind*/SWE: Ogilvie *et al.*, 1995), *Massachusetts Institute of Technology Faraday cup experiment* on IMP-8 (IMP-8/MIT: Bellomo and Mavretic, 1978), and the *Comprehensive Plasma Instrumentation* on GEOTAIL (GEOTAIL/CPI: Frank *et al.*, 1994); these are determined from the NASA/GSFC OMNI dataset through OMNIWeb Plus (http://omniweb.gsfc.nasa.gov/index.html).

Using the values of V_{SOHO}, V_{IPS}, and V_{bg}, we classify the 50 ICMEs into three types: fast ($V_{SOHO} - V_{bg} > 500$ km s^{-1}), moderate (0 km s^{-1} $\leq V_{SOHO} - V_{bg} \leq 500$ km s^{-1}), and slow ($V_{SOHO} - V_{bg} < 0$ km s^{-1}). In our results, the numbers of fast, moderate, and slow ICMEs are 19, 25, and 6, respectively. Here, we eliminate 5 of the 19 fast ICMEs and a moderate ICME because they show an extreme zigzag profile of propagation speeds, *i.e.* $V_1 - V_2 > 1000$ km s^{-1}. The value of $V_1 - V_2 > 1000$ km s^{-1} implies that the ICME has a strange acceleration, and then shows an unrealistic propagation. We also eliminate 4 of the 24 moderate ICMEs and 1 of the 6 slow ones because they exhibit unusual values of V_{IPS} of $V_{IPS} - V_{bg} > 500$ km s^{-1} and $V_{IPS} - V_{bg} > 100$ km s^{-1}, respectively. The values of $V_{IPS} - V_{bg} > 500$ km s^{-1} for moderate and $V_{IPS} - V_{bg} > 100$ km s^{-1} for slow ICMEs imply that the ICME has a strange acceleration since V_{IPS} is larger than V_{SOHO} and V_{Earth}, and an unrealistic ICME propagation that indicates a higher speed in the region beyond coronagraph distances, and less at 1 AU.

Finally, we obtain physical properties for 39 ICMEs which consist of 14 fast, 20 moderate, and 5 slow ones.

4. Results

4.1. Properties and Speed Profiles of the 39 ICMEs

The properties of the 39 ICMEs identified from our analysis are listed in Tables 1 and 2, which include T_{IPS}, R_0, α, β, and V_{Tr} in addition to T_{SOHO}, V_{POS}, V_{SOHO}, R_1, V_1, a_1, R_2, V_2, a_2, T_{Earth}, V_{Earth}, and V_{bg} above. Here, T_{IPS} and R_0 are the mean time and the average radial distance for an ICME detected by IPS observations; those are given as the averages of t_{IPS} and of r_{IPS} for the $g \geq 1.5$ sources, respectively. The α and β are the index and coefficient for a power-law form of the radial speed evolution described as

$$V = \beta R^{\alpha} , \tag{9}$$

where R is the heliocentric distance. V_{Tr} is the transit speed:

$$V_{Tr} = \frac{r_E}{T_{Earth} - T_{SOHO}} . \tag{10}$$

This is equivalent to the average speed of ICMEs between the Sun and the Earth.

In addition, we plot all of the speed profiles in order to show radial speed evolutions of ICMEs in Figure 2. Here, data points for each ICME are connected by solid lines instead of fitting in Equation (9). As shown here, ICME propagation speeds in the near-Sun region exhibit a wide range from 90 km s^{-1} to ≈2100 km s^{-1}, while those in the near-Earth region range from 310 km s^{-1} to 790 km s^{-1}. Moreover, the range of ICME propagation speeds in interplanetary space decreases with increasing distance. In addition, speeds of the background solar wind also show a relatively narrow span from 286 km s^{-1} to 662 km s^{-1}.

4.2. Fast, Moderate, and Slow ICMEs, and Their Accelerations

For the fast, moderate, and slow ICMEs, we show representative examples of speed profiles in Figures 3, 4, and 5, respectively. These are plotted using the values of V_{SOHO}, R_1, V_1, R_2, V_2, V_{Earth}, and V_{bg}. Figure 3 shows a speed profile for a fast ICME observed as a halo by SOHO/LASCO on 5 November 1998, a subsequent disturbance from the IPS observations on

7 November 1998, and the event detected at 1 AU by *in-situ* observations on 9 November 1998 (see No. 4 in Table 1 and 2). These data show that the ICME speed rapidly decreases to the value of V_{bg} with an increase in radial distance; the initial speed V_{SOHO} value is 1342 km s^{-1}, while V_{bg} = 385 km s^{-1} for this ICME. This speed profile is well fit by a power-law function; the fitting-line has a value of $\alpha = -0.478$ from Equation (9). Figure 4 shows the speed profile for a moderate ICME; this ICME was observed as a normal event (neither a halo nor a partial halo) by SOHO/LASCO on 17 July 2000, on 19 July 2000 in IPS, and detected by *in-situ* observations on 20 July 2000 (see No. 14 in Table 1 and 2). As shown here, for this ICME, the 788 km s^{-1} initial speed gradually decreases to V_{bg} = 574 km s^{-1} with an increase in radial distance; we have a value of $\alpha = -0.079$. Figure 5 exhibits a speed profile for a slow ICME observed as a normal event by SOHO/LASCO on 29 May 2009, on 1 June 2009 by IPS observations, and detected by *in-situ* observations on 4 June 2009 (see No. 39 in Table 1 and 2). For this event, we confirm that V_{SOHO} = 139 km s^{-1}, and that the propagation speed increases to V_{bg} = 327 km s^{-1} with radial distance. This ICME shows acceleration, and the fit has a value of $\alpha = 0.276$.

Figure 6 shows the average radial acceleration for groups of fast, moderate, and slow ICMEs; the average acceleration in the two regions [a_1 and a_2] are calculated first using Equations (5) and (6) for each ICME, and each is subsequently averaged for respective groups. For all of them, the mean values of R_1 and R_2 with the standard errors are 0.33 ± 0.04 and 0.79 ± 0.04 AU, respectively. From this figure, we confirm that the acceleration levels vary toward zero with an increase in distance, and this trend is conspicuous for the group of fast ICMEs. We also confirm that the group of moderate ICMEs shows little acceleration.

4.3. Critical Speed for Zero Acceleration

If ICMEs accelerate or decelerate by interaction with the solar wind, we expect that the acceleration will become zero when the propagation speed of ICMEs reaches the speed of the background solar wind. Therefore, it is important to know the ICME propagation speed in this situation in order to verify our expectations. Here, we call this speed "the critical speed for zero acceleration". In Figures 7 and 8, we give information on this critical speed for zero acceleration in two ways. In Figure 7, we show the relationship between initial ICME speeds [V_{SOHO}] and indices [α]. The α indicates the type of ICME motion, *i.e.* the acceleration ($\alpha > 0$), uniform ($\alpha = 0$), and deceleration ($\alpha < 0$). As shown here, α ranges from 0.486 to –0.596 with an increase in V_{SOHO}. Table 3 gives the mean values of the critical speed for zero acceleration [V_{c1}], coefficients [k_1, k_2, and k_3] for the best-fit curve and their standard errors. Figure 8 shows the relationship between ICME speeds [V_{SOHO} and V_{IPS}] and accelerations [a_1 and a_2]. Table 4 presents the mean values of the critical speed for zero acceleration [V_{c2}] slope, and intercept for the best-fit line and their standard errors, which are estimated using the {FITEXY.pro} from the IDL Astronomy User's Library (http://idlastro.gsfc.nasa.gov/homepage.html). From the above examinations, we find $V_{c1} = 471 \pm 19$ km s^{-1} and $V_{c2} = 480 \pm 21$ km s^{-1} as the critical speed for zero acceleration.

4.4. Relationship between Acceleration and Difference in Speed

We investigated how the ICME acceleration relates to the difference in speed between it and the background solar wind. In this investigation, we attempted to show which is more suitable to describe the relationship between acceleration and difference in speed: $a = -\gamma_1(V - V_{bg})$ or $a = -\gamma_2(V - V_{bg})|V - V_{bg}|$; these expressions were introduced and also tested in the earlier study by Vršnak and Gopalswamy (2002). Here, a, V, and V_{bg} denote the acceleration, ICME speed, and speed of the background solar wind, respectively. Although it was assumed that the coefficients [γ_1 and γ_2] decrease with the heliocentric distance in the earlier study, for this analysis we assume that the values of coefficients are constants because we want as few variables as possible to describe the relationship. We also assume that the speed of the background solar wind [V_{bg}] is constant for heliocentric distances ranging from ≈0.1 to 1 AU. This assumption has been verified approximately between 0.3 and 1 AU by Neugebauer (1975) and Schwenn, Mühlhäuser, and Marsch (1981). In Figure 9, the top panel shows the

relationship between a and $(V - V_{bg})$, and the bottom panel that between a and $(V - V_{bg})|V - V_{bg}|$ for ICMEs with $(V_{SOHO} - V_{bg}) \geq 0$ km s^{-1}, *i.e.* the fast and moderate ICMEs. Table 5 exhibits the values of γ_1 and γ_2, correlation coefficients, and reduced χ^2 derived from this analysis. It is noted that the γ_1, γ_2, and χ^2 are calculated using the FITEXY.pro. Although we also examined the slow ICMEs in the same way, we did not obtain a conclusive result. We discuss interpretations of these results in the next section.

5. Discussion

From Figures 2, 3, and 4, we confirm that fast and moderate ICMEs are rapidly and gradually decelerating during their outward propagation, respectively, while slow ICMEs are accelerating, and consequently all attain speeds close to those of the background solar wind. As shown in Figure 5, the distribution of ICME propagation speeds in the near-Sun region is wider than in the near-Earth region for all of the ICMEs identified in this study. This is consistent with the earlier study by Lindsay *et al*. (1999). We also confirm that the distribution of ICME propagation speed in the near-Earth region is similar to that of the background solar-wind speed at 1 AU. We interpret these results as indicating that ICMEs accelerate or decelerate by interaction with the solar wind; the magnitude of the propelling or retarding force acting upon ICMEs depends on the difference between ICMEs and the solar wind. Thus, ICMEs attain final speeds close to the solar-wind speed as they move outward from the Sun. Figure 5 also shows the radial evolution of ICME propagation speeds between 0.08 and 1 AU. We show that ICME speeds reach their final value at 0.79 ± 0.04 AU or at a solar distance slightly less than 1 AU. In addition, we confirm from Figure 6 that the acceleration at 0.79 ± 0.04 AU is much lower than at 0.33 ± 0.04 AU; this is the clearest for the group of fast ICMEs. From this, we thus conclude that most of the ICME acceleration or deceleration ends by 0.79 ± 0.04 AU. This is consistent with an earlier result obtained by Gopalswamy *et al*. (2001).

We expect that the critical speed of zero acceleration will be close to that of the background solar-wind speed on the basis of the above. We derive two different critical speeds of $V_{c1} = 471 \pm 19$ km s^{-1} and of $V_{c2} = 480 \pm 21$ km s^{-1} from the observational data. Although there is agreement between them, both are somewhat higher than the ≈380 km s^{-1} reported to be the threshold speed by Manoharan (2006) and the 405 km s^{-1} reported by Gopalswamy *et al*. (2000). We suggest that this discrepancy is caused by the difference in our analysis methods and also the time interval chosen for the analysis. Because the properties of the background solar wind (*e.g.* speed and density) vary with the change in solar activity, we consider this discrepancy to be minor, and we note that both critical speeds in our result are within the typical speed of the solar wind: $V_{bg} = 445 \pm 95$ km s^{-1} from our sample. Here, we adopt the speed of 480 km s^{-1} as the critical speed for zero acceleration as a mean that is derived from the relationship between propagation speeds and accelerations without the assumption of a power-law form for the motion of the ICME.

Vlasov (1992) and Manoharan (2006) point out that the radial evolution of ICME speeds can be represented by a power-law function. A power-law speed evolution also applies to the ICMEs identified in this study as shown in Figures 2, 3, and 4. As indicated by Figure 7, the value of α varies from 0.499 (acceleration) to –0.596 (strongly deceleration) as ICME speeds increase. This result is consistent with that exhibited in Figure 8.

The relationship between acceleration and speed-difference for ICMEs is usually expressed by either of the following: a linear equation $a = -\gamma_1(V - V_{bg})$ or a quadratic equation $a = -\gamma_2(V - V_{bg})|V - V_{bg}|$. As shown in Figure 9, these equations are evaluated using the acceleration and speed-difference data derived from our observations. From this and Table 5, we find that the reduced χ^2 for the former relationship is smaller than for the latter. The assessment of the significance level shows that $\chi^2 = 1.26$ for the linear equation is smaller than the reduced χ^2 corresponding to the probability of 0.05 with 66 degrees of freedom, while $\chi^2 = 2.90$ for the quadratic one is larger. We therefore conclude that the linear equation is more suitable than the quadratic one to describe the kinematics of ICMEs with $(V_{SOHO} - V_{bg}) \geq 0$ km s^{-1}. From the viewpoint of fluid dynamics, a linear equation suggests the

hydrodynamic Stokes drag force is operating, while the quadratic equation suggests that the aerodynamic drag force. Maloney and Gallagher (2010) found that the acceleration of a fast ICME showed a linear dependence on the speed difference, while that of a slow ICME showed a quadratic dependence. Our conclusion is consistent with their finding only for the fast and moderate ICMEs. We could not verify their result for the slow ICMEs because we lack sufficient observational data for the slow ICMEs in our sample. We expect to make a more detailed examination for the motion of slow ICMEs in a future study.

We also obtained the mean value of 6.58×10^{-6} s^{-1} for the coefficient γ_1 in our analysis. Substituting our value of γ_1 in our linear equation, we obtain the following simple expression:

$$a = -6.58\times10^{-6}\left(V - V_{\rm bg}\right), \tag{11}$$

where a, V, and $V_{\rm bg}$ are the acceleration, ICME propagating speed, and speed of the background solar wind, respectively, as a useful way to determine the dynamics of ICMEs.

Last, we discuss why the linear equation with a constant γ_1 can explain the observational result. Our IPS radio-telescope system observes fluctuations of radio signals. These fluctuations are proportional to the solar-wind (electron) density [*N*e]. Therefore, low-density ICMEs may not be detected by our system. Moreover, we used a threshold *g*-value more severe than that used by Manoharan (2006) or Gapper *et al.* (1982) for identification of ICMEs. Hence, it is conceivable that almost all detected ICMEs are high-density events in this study. In addition, from a theoretical study, Cargill (2004) indicated that with dense ICMEs, the factor $\gamma$and $C_{\rm D}$ (the dimensionless drag coefficient) become approximately constant for aerodynamic drag deceleration; here, $\gamma C_{\rm D} = \gamma_2$ in our notation. From this, we surmise that a constant value of $\gamma C_{\rm D}$ indicates that both interplanetary-space conditions and the properties of dense ICMEs are unchanged in the range from the Sun to the Earth. Therefore, γ_1 must also become approximately constant over the same range from the Sun to the Earth. Thus, to recapitulate, the events detected using our IPS radio-telescope system give results for dense ICMEs, and the dynamics of these are well explained by a linear equation with γ_1 = constant.

6. Summary and Conclusions

We investigate radial evolution of propagation speed for 39 ICMEs detected by SOHO/LASCO, IPS at 327 MHz, and *in-situ* observations during 1997 – 2009 covering nearly all of Solar Cycle 23. In this study, we first analyze *g*-values obtained by STEL IPS observations in the above period, and find 497 IPS disturbance event days (IDEDs) as candidates for ICME events. Next, we compare the list of these IDEDs with that of CME/ICME pairs observed by SOHO/LASCO and *in-situ* observations, and finally we are left with 50 ICMEs; those ICMEs that traveled from the Sun to the Earth, and were detected at three locations between the Sun and the Earth's orbit, *i.e.* near-Sun, interplanetary space, and near-Earth. For these ICMEs, we determine reference distances and derive the propagation speeds and accelerations in the SOHO–IPS and IPS–Earth regions. Our examinations yield the following results.

i) Fast ICMEs (with $V_{\rm SOHO} - V_{\rm bg} > 500$ km s^{-1}) rapidly decelerate, moderate ICMEs (with 0 km s^{-1} $\leq V_{\rm SOHO} - V_{\rm bg} \leq 500$ km s^{-1}) show either gradually deceleration or uniform motion, while slow ICMEs (with $V_{\rm SOHO} - V_{\rm bg} < 0$ km s^{-1}) accelerate, where $V_{\rm SOHO}$ and $V_{\rm bg}$ are the initial speed of ICME and the speed of the background solar wind, respectively. Consequently, radial speeds converge to the speed of the background solar wind during their outward propagation. Thus, the distribution of ICME propagation speeds in the near-Earth region is narrower than in the near-Sun region as shown in Figure 5. This is consistent with the earlier study by Lindsay *et al*. (1999).

ii) Both the ICME accelerations and the decelerations are nearly complete by 0.79 ± 0.04 AU. This is consistent with an earlier result obtained by Gopalswamy *et al*. (2001). Both critical speeds (where the speed of ICME acceleration becomes zero) derived from our analysis, *i.e.* 471 ± 19 km s^{-1} and 480 ± 21 km s^{-1}, are somewhat higher than the values

reported by Manoharan (2006) and Gopalswamy *et al.* (2000). However, this discrepancy is most likely explained because our analysis methods and data collection periods are different. Both critical speeds in our result do not differ much from the typical speed of the solar wind, and we adopt the mean value of 480 km s^{-1} as the critical speed for zero acceleration. This is close to the speed of the background solar wind, V_{bg} = 445 ± 95 km s^{-1}, during this period of study.

iii) For ICMEs with $(V_{SOHO} - V_{bg}) \geq 0$ km s^{-1}, a linear equation $a = -\gamma_1(V - V_{bg})$ with $\gamma_1 = 6.58 \pm 0.23 \times 10^{-6}$ s^{-1} is more appropriate than a quadratic equation $a = -\gamma_2(V - V_{bg})|V - V_{bg}|$ to describe their kinematics, where γ_1 and γ_2 are coefficients, a, V, and V_{bg} are the acceleration and propagation speed of ICMEs, and the speed of the background solar wind, respectively, because the reduced χ^2 for the linear equation satisfies the statistical significance level at 0.05, while the quadratic one does not.

These results support our assumption that ICMEs are accelerated or decelerated by a drag force caused by an interaction with the solar wind; the magnitude of the drag force acting upon ICMEs depends on the difference in speed, and, thus, ICMEs attain final speeds close to the solar-wind speed when the force becomes zero. In particular, our result *iii*) suggests that ICMEs propagating faster than the background solar wind are controlled mainly by the hydrodynamic Stokes drag force. Moreover, our result *iii*) confirms the finding by Maloney and Gallagher (2010) only for the fast and moderate ICMEs that we measure. From the characteristics of the IPS observations and the result of Cargill (2004), we conclude that the ICMEs detected by the IPS observations in this study are probably high-density events. A combination of the space-borne coronagraph, ground-based IPS, and satellite *in-situ* observations serves to detect many ICMEs between the Sun and the Earth, and is a useful means to study their kinematics.

Acknowledgments The IPS observations were carried out under the solar-wind program of the Solar-Terrestrial Environment Laboratory (STEL) of Nagoya University. We acknowledge use of the SOHO/LASCO CME catalog; this CME catalog is generated and maintained at the CDAW Data Center by NASA and the Catholic University of America in cooperation with the Naval Research Laboratory. SOHO is a project of international cooperation between ESA and NASA. We thank NASA/GSFC's Space Physics Data Facility for use of the OMNIWeb service and OMNI data. We thank the IDL Astronomy User's Library for the use of IDL software. We acknowledge use of the comprehensive ICME catalog compiled by I.G. Richardson and H.V. Cane. We also thank B.V. Jackson for useful help and comments.

References

Andrews, M.D.: 2001, LASCO and EIT observations of the Bastille Day 2000 solar storm, *Solar Phys.* **204**, 181. doi:10.1023/A:1014215923912

Asai, K., Ishida, Y., Kojima, M., Maruyama, K., Misawa, H., Yoshimi, N.: 1995, Multi-station system for solar wind observations using the interplanetary scintillation method, *J. Geomag. Geoelectr.* **47**, 1107.

Bellomo, A., Mavretic, A.: 1978, MIT plasma experiment on IMP H and J Earth orbited satellites, *MIT Center for Space Research Technical Report CSR-TR-78-2*.

Bisi, M.M., Breen, A. R., Jackson, B.V., Fallows, R.A., Walsh, A.P., Mikić, Z., Riley, P., Owen, C.J., Gonzalez-Esparza, A., Aguilar-Rodriguez, E., *et al.*: 2010, From the Sun to the Earth: The 13 May 2005 Coronal Mass Ejection, *Solar Phys.* **265**, 49. doi: 10.1007/s11207-010-9602-8.

Brueckner, G.E., Howard, R.A., Kooman, M.J., Korendyke, C.M., Michels, D.J., Moses, J.D., Socker, D.G., Dere, K.P., Lamy, P.L., Llebaria, A., *et al.*: 1995, The large angle spectroscopic coronagraph (LASCO), *Solar Phys.* **162**, 357. doi:10.1007/BF00733434.

Cargill, P.J.: 2004, On the aerodynamic drag force acting on interplanetary coronal mass ejections, *Solar Phys.* **221**, 135. doi:10.1023/B:SOLA-0000033366-10725-a2.

Chen, J.: 1996, Theory of prominence eruption and propagation: Interplanetary

consequences, *J. Geophys. Res.* **101**, A12, 27499. doi:10.1029/96JA02644.
Coles, W.A., Harmon, J.K., Lazarus, A.J., Sullivan, J.D.: 1978, Comparison of 74-MHz interplanetary scintillation and IMP 7 observations of the solar wind during 1973, *J. Geophys. Res.* **83**, A7, 3337. doi:10.1029/JA083iA07p03337.
Frank, L.A., Ackerson, K.L., Paterson, W.R., Lee, J.A., English, M.R., Pickett, G.L.: 1994, The Comprehensive Plasma Instrumentation (CPI) for the GEOTAIL Spacecraft, *J.Geomag. Geoelectr.* **46**, 23.
Gapper, G.R., Hewish, A., Purvis, A., Duffett-Smith, P.J.: 1982, Observing interplanetary disturbances from the ground, *Nature* **296**, 633. doi:10.1038/296633a0.
Gopalswamy, N., Lara, A., Lepping, R.P., Kaiser, M.L., Berdichevsky, D., St. Cyr, O.C.: 2000, Interplanetary acceleration of coronal mass ejections, *Geophys. Res. Lett.* **27**, 2, 145. doi:10.1029/1999GL003639.
Gopalswamy, N., Lara, A., Yashiro, S., Kaiser, M.L., Howard, R.A.: 2001, Predicting the 1-AU arrival times of coronal mass ejections, *J. Geophys. Res.* **106**, A12, 29207. doi:10.1029/2001JA000177.
Gopalswamy, N., Yashiro, S., Liu, Y., Michalek, G., Vourlidas, A., Kaiser, M.L., Howard, R.A.: 2005, Coronal mass ejections and other extreme characteristics of the 2003 October-November solar eruptions, *J. Geophys. Res.* **110**, A09S15. doi: 10.1029/2004JA010958. doi:10.1029/2004JA010958.
Gopalswamy, N., Yashiro, S., Micharek, G., Stenborg, G., Vouridas, A., Freeland, S., Howard, R.: 2009, The SOHO/LASCO CME Catalog, *Earth Moon Planet* **104**, 295. doi:10.1007/s11038-008-9282-7.
Gosling, J.T., Hildner, E., MacQueen, R.M., Munro, R.H., Poland, A.I., Ross, C.L. : 1974, Mass ejections from the Sun: a view from Skylab, *J. Geophys. Res.* **79**, 31, 4581. doi:10.1029/JA079i031p04581.
Gosling, J.T., Bame, S.T., McComas, D.J., Phillips, J.L.: 1990, Coronal mass ejections and large geomagnetic storms, *Geophys. Res. Lett.* **17**, 7, 901. doi:10.1029/GL017i007p00901.
Hewish, A., Scott, P. F., Wills, D.: 1964, Interplanetary scintillation of small diameter radio sources, *Nature* **203**, 4951, 1214. doi:10.1038/2031214a0.
Hewish, A., Bravo, S.: 1986, The sources of large-scale heliospheric disturbances, *Solar Phys.* **106**, 185. doi:10.1007/BF00161362.
Jackson, B.V., Hick, P.P.: 2002, Corotational tomography of heliospheric features using global Thomson scattering data, *Solar Phys.* **211**, 345. doi:10.1023/A:1022409530466.
Jackson, B.V., Hick, P.P., Buffington, A., Bisi, M.M., Clover, J.M., Tokumaru, M., Kojima, M., Fujiki, K.: 2011, Three-dimensional reconstruction of heliospheric structure using iterative tomography: A review, *J. Atoms. Solor-Terr. Phys.* **73**, 1214. doi:10.1016/j.jastp.2010.10.007.
Kojima, M., Kakinuma, T.: 1990, Solar cycle dependence of global distribution of solar wind speed, *Space Sci. Rev.* **53**, 173. doi:10.1007/BF00212754.
Lindsay, G.M., Luhmann, J.G., Russell, C.T., Gosling, J.T.: 1999, Relationships between coronal mass ejection speeds from coronagraph images and interplanetary characteristics of associated interplanetary coronal mass ejections, *J. Geophys. Res.* **104**, A6, 12515. doi:10.1029/1999JA900051.
McComas, D.J., Bame, S.J., Barker, P., Feldman, W.C., Phillips, J.L., Riley, P., Griffee, J.W.: 1998, Solar wind electron proton alpha monitor (SWEPAM) for the Advanced Composition Explorer, S*pace Sci. Rev.* **86**, 563. doi:10.1023/A:1005040232597.
Maloney, S.A., Gallagher, P.T.: 2010, Solar wind drag and the kinematics of interplanetary coronal mass ejections, *Astrophys. J. Lett.* **724**, L127. doi: 10.1088/2041-8205/724/2/L127
Manoharan, P.K.: 2006, Evolution of coronal mass ejections in the inner heliosphere: a study using white-light and scintillation images, *Solar Phys.* **235**, 345. doi: 10.1007/s11207-006-0100-y.
Manoharan, P.K.: 2010, Ooty Interplanetary Scintillation – Remote-Sensing Observations and Analysis of Coronal Mass Ejections in the Heliosphere, *Solar Phys.* **265**, 137. doi: 10.1007/s11207-010-9593-5.

Manoharan, P.K., Kojima, M., Gopalswamy, N., Kondo, T., Smith, Z.: 2000, Radial evolution and turbulence characteristics of a coronal mass ejection, *Astrophys. J.* **530**, 1061. doi:10.1086/308378.

Michalek, G., Gopalswamy, N., Yashiro, S.: 2003, A new method for estimating widths, velocities, and source location of halo coronal mass ejections, *Astrophys. J.* **584**, 472. doi:10.1086/345526.

Neugebauer, M.: 1975, Large-scale and solar-cycle variations of the solar wind, *Space Sci. Rev.* **17**, 221. doi:10.1007/BF00718575.

Ogilvie, K.W., Chornay, D.J., Fritzenreiter, R.J., Hunsaker, F., Keller, J., Lobell, J., Miller, G., Scudder, J.D., Sittler, Jr., E.C., Torbert, R.B., *et al.*: 1995, SWE, A comprehensive plasma instrument for the Wind spacecraft, *Space Sci. Rev.* **71**, 55. doi:10.1007/BF00751326.

Ontiveros, V., Vourlidas, A.: 2009, Quantitative Measurements of Coronal Mass Ejection-Driven Shocks from LASCO Observations, *Astrophys. J.* **693**, 267. doi: 10.1088/0004-637X/693/1/267.

Reiner, M.J., Kaiser, M.L., Bougeret, J.L.: 2007, Coronal and interplanetary propagation of CME/Shocks from radio, in situ and white-light observations, *Astrophys. J.* **663**, 1369. doi:10.1086/518683.

Richardson, I.G., Cane, H.V.: 2010, Near-Earth interplanetary coronal mass ejections during solar cycle 23 (1996 – 2009): catalog and summary of properties, *Solar Phys.* **264**, 189. doi: 10.1007/s11207-010-9568-6.

Schwenn, R.: 1983, Direct correlations between coronal transients and interplanetary disturbances, *Space Sci. Rev.* **34**, 85. doi:10.1007/BF00221199.

Schwenn, R., Mühlhäuser, K.H., Marsch, E.: 1981, In: Rosenbauer, H. (ed.), *Solar Wind Four,* Max-Planck-Inst. f. Aeronomie, Katlenburg-Lindau, 126.

Stone, E.C., Frandsen, A.M., Mewaldt, R.A., Christian, E.R., Margolies, D., Ormes, J. F., Snow, F.: 1998, The advanced composition explorer, *Space Sci. Rev.* **86**, 1. doi:10.1023/A:1005082526237.

Tappin, S.J.: 2006, The deceleration of an interplanetary transient from the Sun to 5 AU, *Solar Phys.* **233**, 233. doi: 10.1007/s11207-006-2065-2.

Tappin, S.J., Hewish, A., Gapper, G.R.: 1983, Tracking a major interplanetary disturbance, *Planet. Space. Sci.* **31**, 10, 1171. doi:10.1016/0032-0633(83)90106-X.

Temmer, M., Rollet, T., Möstl, C., Veronig, A., Vršnak, B., Odstrčil, D.: 2011, Influence of the ambient solar wind flow on the propagation behavior of interplanetary coronal mass ejections, *Astrophys. J.* **743**, 101. doi:10.1088/0004-637X/743/2/101.

Tokumaru, M., Kojima, M., Fujiki, K., Yokobe, A.: 2000a, Three-dimensional propagation of interplanetary disturbances detected with radio scintillation measurements at 327 MHz, *J. Geophys. Res.* **105**, A5, 10435. doi:10.1029/2000JA900001.

Tokumaru, M., Kojima, M., Ishida, Y., Ohmi, T.: 2000b, Large-scale structure of solar wind turbulence near solar activity minimum, *Adv. Space. Res.* **25**, 9, 1943. doi:10.1016/S0273-1177(99)00630-4.

Tokumaru, M., Kojima, M., Fujiki, K., Yamashita, M., Yokobe, A.: 2003, Toroidal-shaped interplanetary disturbance associated with the halo coronal mass ejection event on 14 July 2000, *J. Geophys. Res.* **108**, A5, 1220, doi: 10.1029/2002JA009574.

Tokumaru, M., Kojima, M., Fujiki, K., Yamashita, M.: 2006, Tracking heliospheric disturbances by interplanetary scintillation, *Nonlin. Processes Geophys.* **13**, 329.

Tsurutani, B.T., Gonzalez, W.D., Tang, F., Akasofu, S., Smith, E.J.: 1988, Origin of interplanetary southward magnetic fields responsible for major magnetic storms near solar maximum (1978 – 1979), *J. Geophys. Res.* **93**, 48, 8519. doi:10.1029/JA093iA08p08519.

Vlasov, V.I.: 1992, In: Marsch, E., Schwenn, R. (ed.), *Solar Wind Seven; Proc. 3rd COSPAR Symp.,* Pergamon, New York, 301.

Vourlidas, A., Lynch, B.J., Howard, R.A., Li, Y.: 2012, How Many CMEs Have Flux Rope? Deciphering the Signatures of Shocks, Flux Ropes, and Prominences in Coronagraph Observations of CMEs, *Solar Phys.*. doi: 10.1007/s11207-012-0084-8.

Vršnak, B., Gopalswamy, N.: 2002, Influence of the aerodynamic drag on the motion of interplanetary ejecta, *J. Geophys. Res.* **107**, A2, 1019. doi:10.1029/2001JA000120.

Watanabe, T., Kakimuma, T.: 1986, Three-dimensional properties of interplanetary

disturbances in 1978 – 1981, *Astrophys. Space Sci.* **118**, 153. doi:10.1007/BF00651120.

Watanabe, T., Schwenn, R.: 1989, Large-scale propagation properties of interplanetary disturbances revealed from IPS and spacecraft observations, *Space. Sci. Rev.* **51**, 147. doi:10.1007/BF00226272.

Woo, R.: 1988, A synoptic study of Doppler scintillation transients in the solar wind, *J. Geophys. Res.* **93**, A5, 3919. doi:10.1029/JA093iA05p03919.

Yashiro, S., Gopalswamy, N., Michalek, G., St. Cyr, O.C., Plunkett, S.P., Rich, N.B., Howard, R.A.: 2004, A catalog of white light coronal mass ejections observed by the SOHO spacecraft, *J. Geophys. Res.* **109**, A07105. doi: 10.1029/2003JA010282.

Young, A. T.: 1971, Interpretation of interplanetary scintillations, *Astrophys. J.* **168**, 543. doi:10.1086/151108.

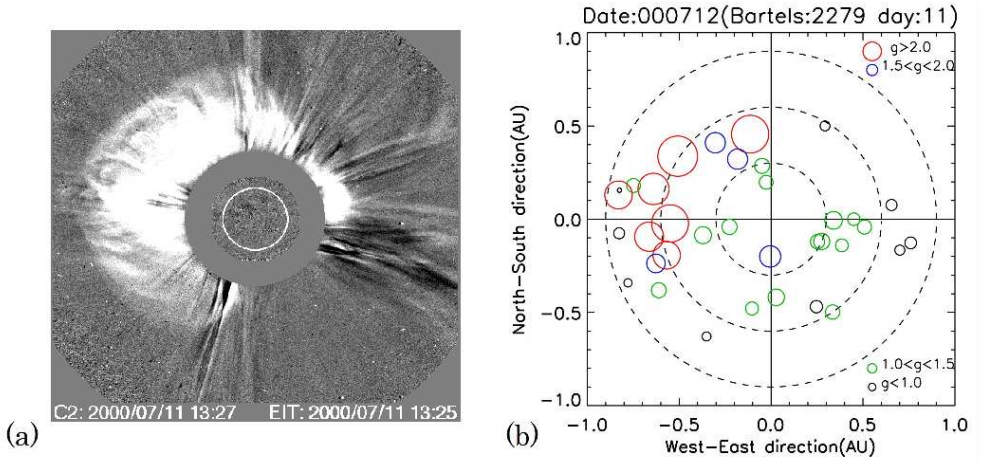

Figure 1 (a) White-light difference image for the halo CME on 11 July 2000 from the SOHO/LASCO-C2 coronagraph (http://cdaw.gsfc.nasa.gov/CME_list/index.html), and (b) *g*-map obtained from our IPS observations on 12 July 2000. The *g*-map center corresponds to the location of the Sun, and concentric circles indicate radial distances of 0.3 AU, 0.6 AU, and 0.9 AU. Colored open solid circles indicate the locations of the closest point to the Sun (the P-point) on the LOS for the radio sources in the sky plane. The center of the colored circle indicates the heliocentric distance of the P-point on the LOS, and color and diameter represent the *g*-value level for each source. We use four bins of $g < 1.0$ (black), $1.0 < g < 1.5$ (green), $1.5 < g < 2.0$ (blue), and $g > 2.0$ (red) for the *g*-map. A group of P-points with red or blue circles indicates a disturbance related to the 11 July 2000 CME.

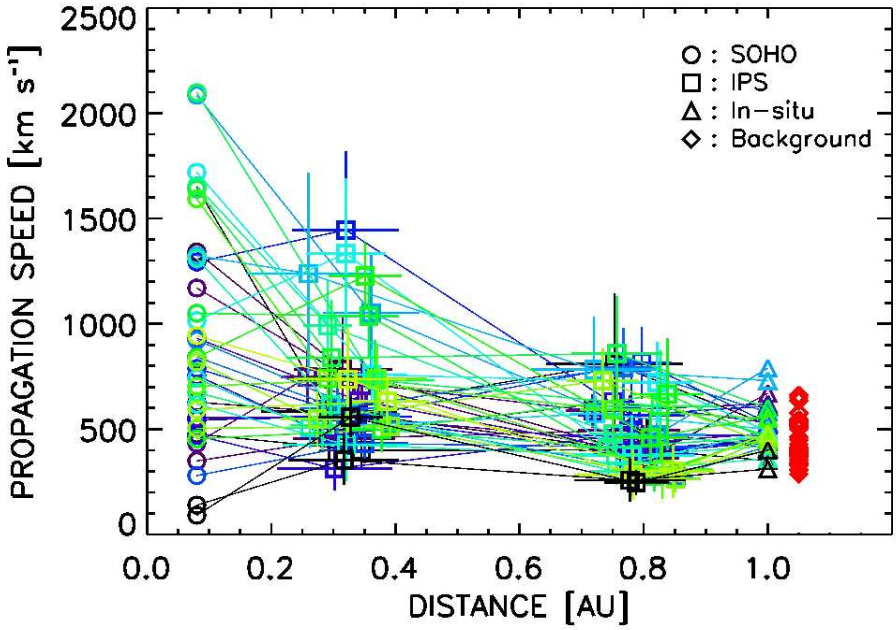

Figure 2 Radial evolution of propagation speeds for the 39 ICMEs in this study. Open circle, square, and triangle symbols indicate speeds of ICMEs measured by SOHO/LASCO, IPS, and *in-situ* observations, respectively. Symbols for each ICME are connected by solid lines with the same color. Open diamond (red) symbols indicate speeds of the background solar wind measured from *in-situ* observations at 1 AU.

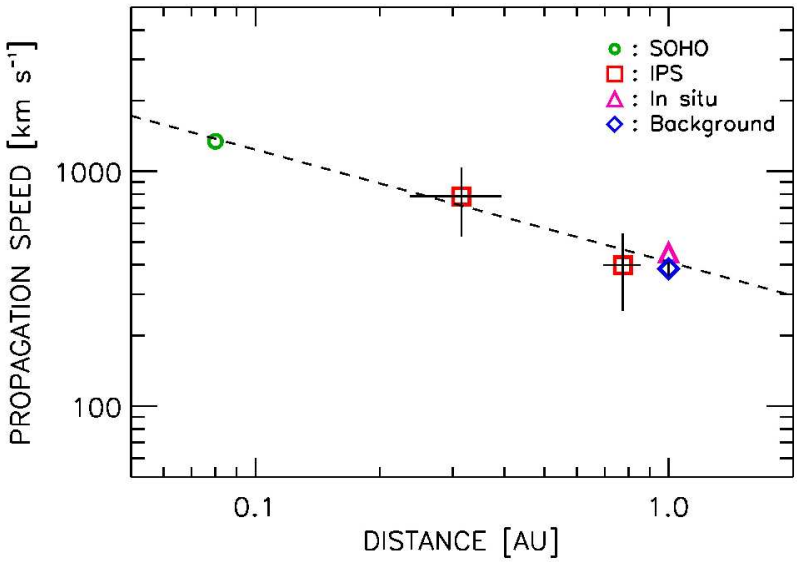

Figure 3 Speed profile for the ICME event between 5 and 9 November 1998. This is an example of a fast ICME. In this event, IPS disturbance event day is 7 November 1998. Open circle, square, and triangle denote measurements of ICME speed from SOHO/LASCO, IPS, and *in-situ* observations, respectively. An open diamond indicates the speed of the background solar wind measured by *in-situ* observations, and the dashed line represents the power-law fit to the data using Equation (9). Horizontal and vertical error bars are also plotted using σ values (standard error) for the reference distances [R_1 and R_2] and those for the speeds [V_1, V_2, and V_{bg}].

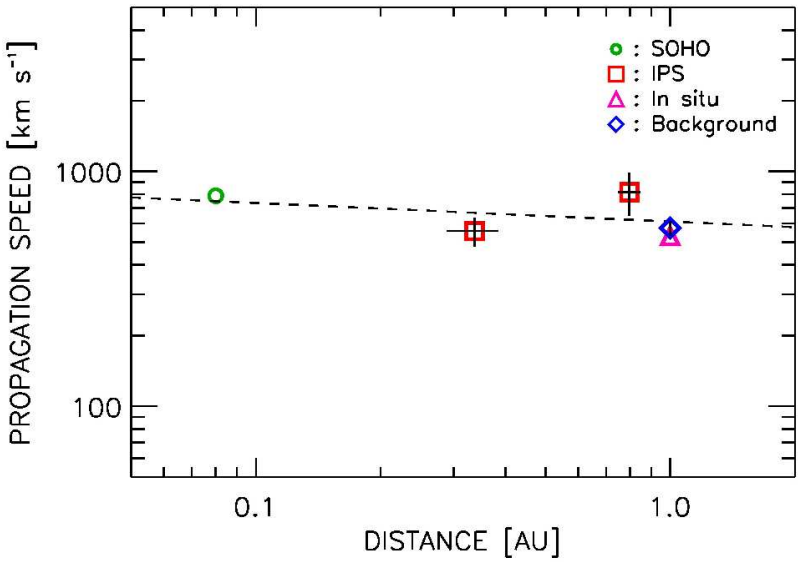

Figure 4 Speed profile for the ICME event between 17 and 20 July 2000. This is an example of a moderate ICME. In this event, IPS disturbance event day is 19 July 2000. Open circle, square, and triangle denote measurements of ICME speed from SOHO/LASCO, IPS, and *in-situ* observations, respectively. An open diamond indicates the speed of the background solar wind measured by *in-situ* observations, and a dashed line represents the power-law fit to the data using Equation (9).

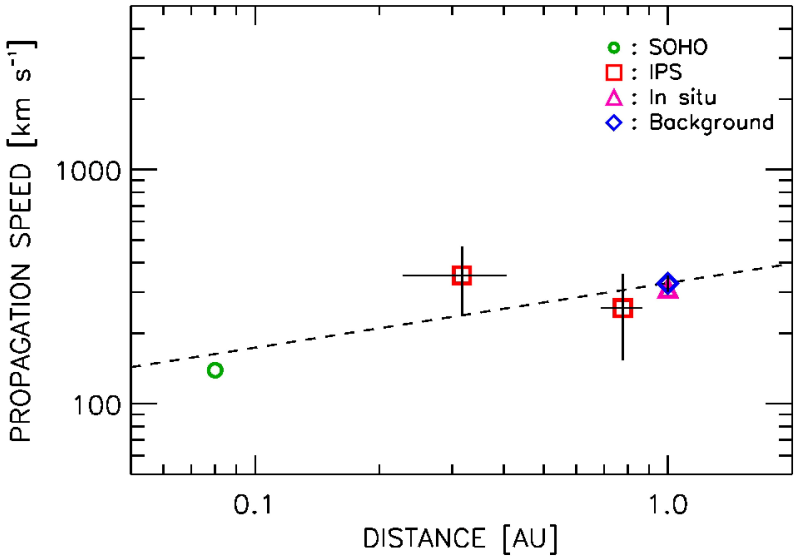

Figure 5 Speed profile for the ICME event between 29 May and 4 June 2009. This is an example of a slow ICME. In this event, IPS disturbance event day is 1 June 2009. Open circle, square, and triangle denote measurements of ICME speed from SOHO/LASCO, IPS, and *in-situ* observations, respectively. An open diamond indicates the speed of the background solar wind measured by *in-situ* observations, and a dashed line represents the power-law fit to the data using Equation (9).

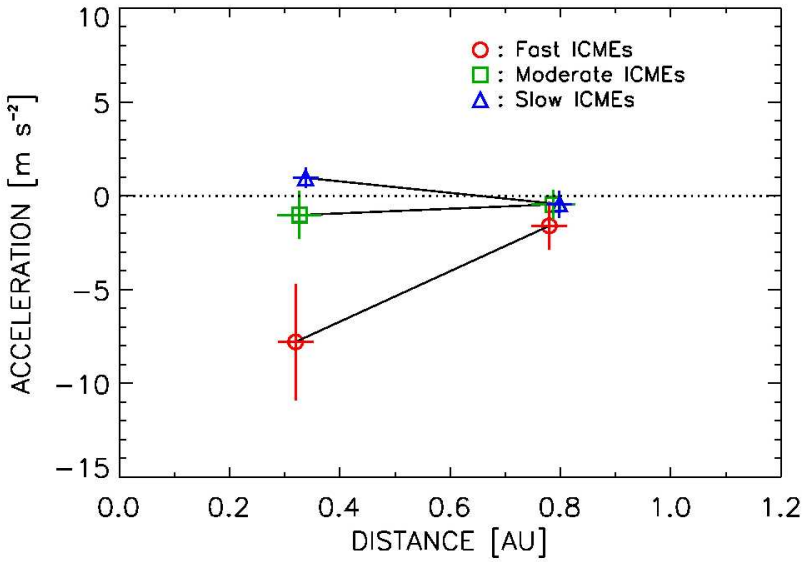

Figure 6 Average radial evolution of acceleration for the fast ($V_{SOHO} - V_{bg} > 500$ km s^{-1}), moderate (0 km s$^{-1} \leq V_{SOHO} - V_{bg} \leq 500$ km s^{-1}), and slow ($V_{SOHO} - V_{bg} < 0$ km s^{-1}) ICMEs in this study. Average accelerations are derived from Equations (5) and (6) with reference distances [R_1 and R_2] for each ICME. Open circle, square, and triangle symbols indicate data points that consist of [R_1, a_1] and [R_2, a_2] averaged for 14 fast, 20 moderate, and 5 slow ICMEs, respectively. Pairs of symbols are connected by solid lines.

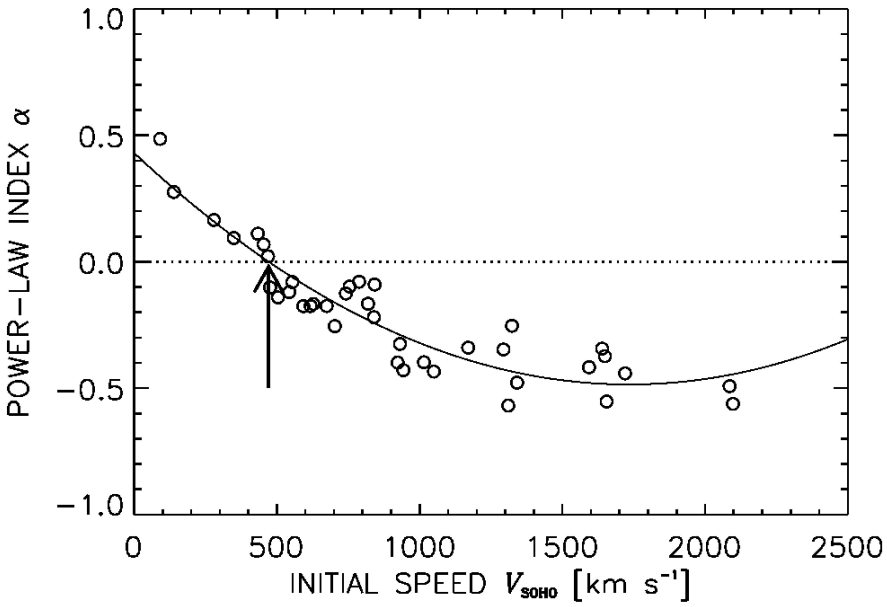

Figure 7 Relationship between estimated initial speeds [V_{SOHO}] and indices [α] for Equation (9) for the 39 ICMEs in this study. Solid and dotted lines show the best-fit quadratic curve $\alpha = k_1 + k_2 V_{SOHO} + k_3 V_{SOHO}^2$ and the $\alpha = 0$ line. The intersection point of these lines is indicated by an arrow, and corresponds to the critical speed for zero acceleration [V_{c1}], which is 471 ± 19 km s^{-1}.

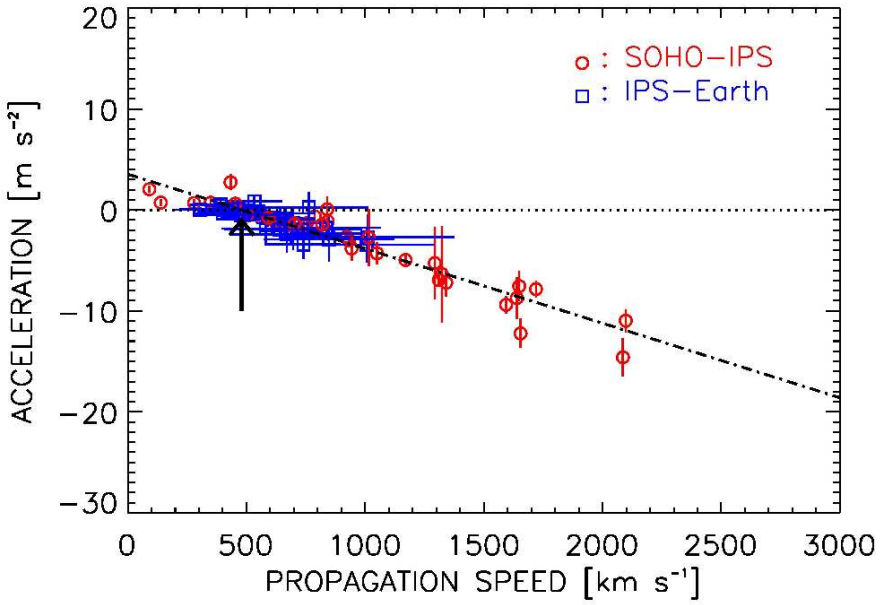

Figure 8 Relationship between propagation speeds and accelerations for the 39 ICMEs in this study. Accelerations are derived from Equations (5) and (6), while values of V_{SOHO} and V_{IPS} are used for the propagation speeds. Open circle and square symbols denote data points, which are [V_{SOHO}, a_1] for the SOHO–IPS region and [V_{IPS}, a_2] for the IPS–Earth region, respectively. Dash–dotted and dotted lines show the best-fit line and zero acceleration line, respectively. The arrow indicates the critical speed for zero acceleration [V_{c2}], which is 480 ± 21 km s^{-1}.

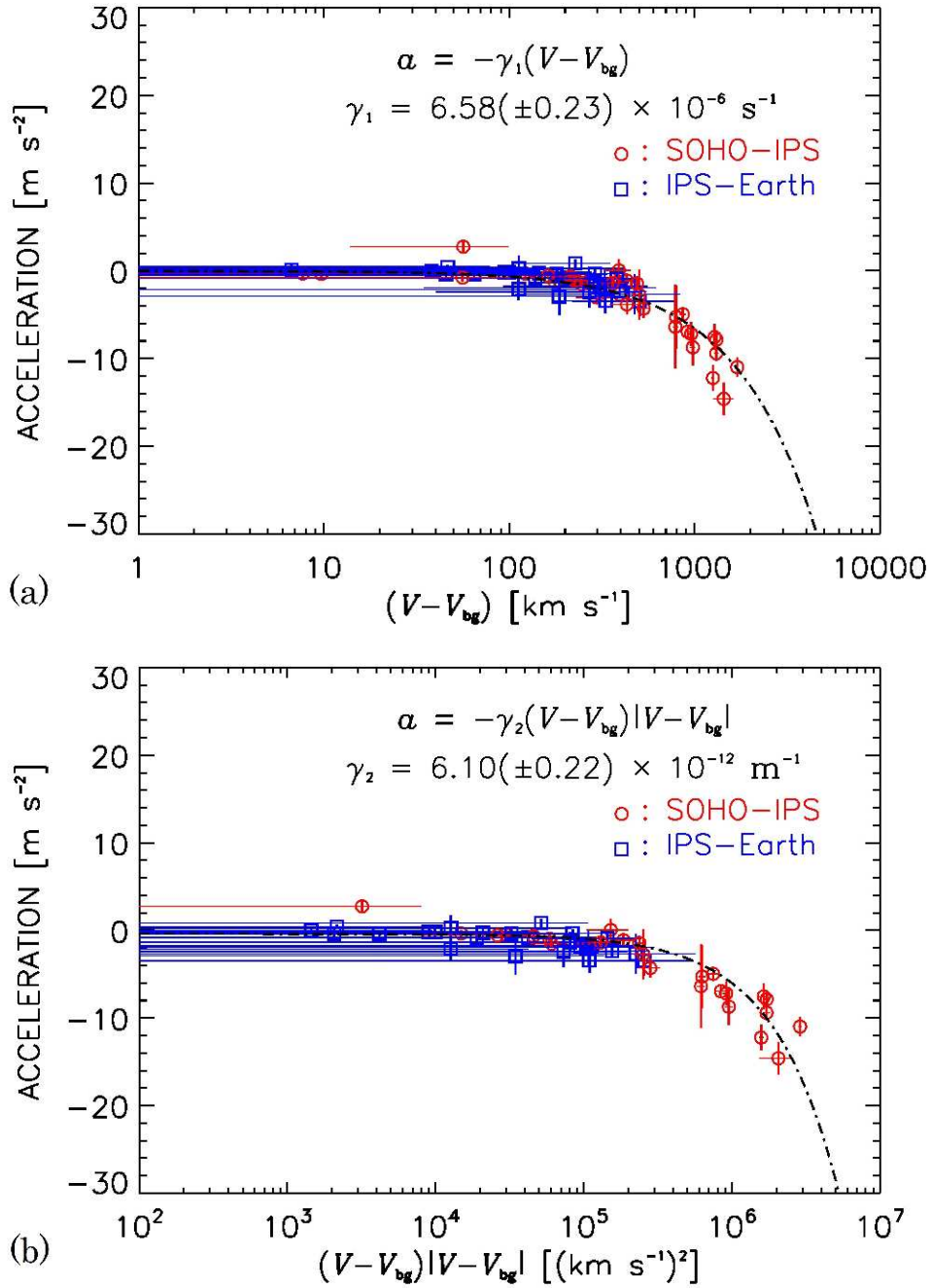

Figure 9 (a) Relationship between acceleration [a] and speed difference [$V - V_{bg}$], and (b) that between a and $(V - V_{bg})|V - V_{bg}|$, for 34 of the fast and moderate ICMEs (*i.e.* $V_{SOHO} - V_{bg} \geq 0$ km s^{-1}) in this study. Open circle and square symbols denote data points that consist of values of ($V_{SOHO} - V_{bg}$) and a_1 [or $(V_{SOHO} - V_{bg})|V_{SOHO} - V_{bg}|$ and a_1] for the SOHO–IPS region and those in which consist of values of ($V_{IPS} - V_{bg}$) and a_2 [or $(V_{IPS} - V_{bg})|V_{IPS} - V_{bg}|$ and a_2] for the IPS–Earth region, respectively. In each panel, the dash–dotted curve denotes the best-fit line shown as a curve because of the logarithmic x-axis scale.

Table 1 Properties derived from SOHO/LASCO observations and those in the SOHO–IPS region derived from IPS observations for 39 ICMEs during 1997 – 2009.

	SOHO/LASCO						IPS									
									Disturbance				SOHO–IPS region			
	Date	Time	V_{POS}	V_{SOHO}	CME	PA	Date	Time	R_0[AU]		R_1[AU]		V_1[km s^{-1}]		a_1 [m s^{-2}]	
No.	[ddmmmyy]	[hhmm]	[km s^{-1}]	[km s^{-1}]	Type	[deg]	[ddmmmyy]	[hhmm]	Aver.	σ	Aver.	σ	Aver.	σ	Aver.	σ
1	06 Dec 1997	1027	397	476	PH	317	09 Dec 1997	0115	0.61	0.13	0.35	0.07	399	93	−0.34	0.36
2	29 Apr 1998	1658	1374	1649	FH	−99	01 May 1998	0358	0.51	0.22	0.29	0.11	584	243	−7.55	1.47
3	04 Nov 1998	0754	523	628	FH	−99	06 Nov 1998	0259	0.60	0.10	0.34	0.05	570	116	−0.95	0.45
4	05 Nov 1998	2044	1118	1342	FH	−99	07 Nov 1998	0143	0.55	0.16	0.32	0.08	782	257	−7.20	1.36
5	13 Apr 1999	0330	291	349	PH	228	15 Apr 1999	0453	0.55	0.16	0.32	0.08	456	130	0.71	0.55
6	24 Jun 1999	1331	975	1170	FH	−99	26 Jun 1999	0114	0.61	0.10	0.35	0.05	705	135	−4.96	0.61
7	28 Jul 1999	0430	361	433	PH	112	29 Jul 1999	0408	0.44	0.09	0.26	0.04	747	135	2.74	0.79
8	28 Jul 1999	0906	462	554	FH	−99	30 Jul 1999	0438	0.60	0.12	0.34	0.06	557	97	−0.37	0.43
9	17 Aug 1999	1331	776	931	PH	61	19 Aug 1999	0403	0.60	0.14	0.34	0.07	635	138	−3.04	0.67
10	21 May 2000	0726	629	755	PH	304	23 May 2000	0311	0.50	0.07	0.29	0.03	469	60	−1.31	0.29
11	31 May 2000	0806	391	469	PH	46	03 Jun 2000	0417	0.52	0.18	0.30	0.09	312	105	−0.32	0.37
12	07 Jul 2000	1026	453	544	FH	−99	09 Jul 2000	0345	0.57	0.20	0.33	0.10	559	180	−0.49	0.80
13	11 Jul 2000	1327	1078	1294	FH	−99	12 Jul 2000	0459	0.56	0.17	0.32	0.09	1446	373	−5.27	3.60
14	17 Jul 2000	0854	788	788	NM	95	19 Jul 2000	0421	0.59	0.10	0.34	0.05	557	78	−0.65	0.56
15	06 Aug 2000	1830	233	280	PH	105	09 Aug 2000	0503	0.62	0.14	0.35	0.07	432	95	0.68	0.40
16	09 Aug 2000	1630	702	842	FH	−99	11 Aug 2000	0446	0.54	0.12	0.31	0.06	600	123	−1.12	0.78
17	29 Aug 2000	1830	769	923	PH	347	01 Sep 2000	0106	0.70	0.06	0.39	0.03	530	57	−2.65	0.19
18	08 Nov 2000	2306	1738	2086	PH	271	10 Nov 2000	0017	0.64	0.16	0.36	0.08	1053	283	−14.60	1.88
19	11 Apr 2001	1331	1103	1324	FH	−99	12 Apr 2001	0334	0.44	0.20	0.26	0.10	1239	477	−6.38	4.77
20	14 Aug 2001	1601	618	742	FH	−99	16 Aug 2001	0341	0.44	0.08	0.26	0.04	507	97	−1.57	0.45
21	25 Aug 2001	1650	1433	1720	FH	−99	27 Aug 2001	0337	0.64	0.11	0.36	0.06	758	122	−7.85	0.85
22	28 Sep 2001	0854	846	1015	FH	−99	29 Sep 2001	0220	0.56	0.13	0.32	0.06	1334	359	−2.72	2.84
23	22 Oct 2001	1826	618	618	NM	131	25 Oct 2001	0116	0.56	0.20	0.32	0.10	425	171	−1.11	0.58
24	25 Oct 2001	1526	1092	1310	FH	−99	27 Oct 2001	0137	0.51	0.09	0.30	0.04	617	136	−6.94	0.55
25	17 Nov 2001	0530	1379	1655	FH	−99	18 Nov 2001	0229	0.50	0.08	0.29	0.04	991	222	−12.23	1.45

Table1 (Continued)

	SOHO/LASCO						IPS									
									Disturbance				SOHO–IPS region			
	Date	Time	V_{POS}	V_{SOHO}	CME	PA	Date	Time	R_0 [AU]		R_1 [AU]		V_1 [km s^{-1}]		a_1 [m s^{-2}]	
No.	[ddmmmyy]	[hhmm]	[km s^{-1}]	[km s^{-1}]	Type	[deg]	[ddmmmyy]	[hhmm]	Aver.	σ	Aver.	σ	Aver.	σ	Aver.	σ
26	29 Jul 2002	1207	562	674	PH	13	31 Jul 2002	0212	0.48	0.10	0.28	0.05	519	117	−1.52	0.47
27	05 Sep 2002	1654	1748	2098	FH	−99	07 Sep 2002	0503	0.65	0.19	0.37	0.10	733	192	−10.98	1.13
28	28 May 2003	0050	1366	1639	FH	−99	29 May 2003	0210	0.51	0.15	0.30	0.07	838	275	−8.72	2.05
29	14 Jun 2003	0154	875	1050	PH	26	15 Jun 2003	0311	0.63	0.10	0.36	0.05	1038	194	−4.30	1.10
30	14 Aug 2003	2006	378	454	FH	−99	17 Aug 2003	0409	0.68	0.12	0.38	0.06	497	106	0.62	0.63
31	22 Jul 2004	0731	700	840	PH	66	23 Jul 2004	0406	0.62	0.12	0.35	0.06	1228	158	0.06	1.28
32	12 Sep 2004	0036	1328	1594	FH	−99	13 Sep 2004	0405	0.50	0.11	0.29	0.05	741	138	−9.40	0.84
33	26 May 2005	1506	586	703	FH	−99	28 May 2005	0334	0.66	0.16	0.37	0.08	738	161	−1.38	0.75
34	26 May 2005	2126	420	504	PH	144	29 May 2005	0522	0.70	0.08	0.39	0.04	513	49	−0.57	0.18
35	07 Jul 2005	1706	683	820	FH	−99	09 Jul 2005	0347	0.47	0.12	0.27	0.06	549	132	−1.44	0.74
36	05 Aug 2005	0854	494	593	PH	23	07 Aug 2005	0547	0.69	0.13	0.39	0.07	632	115	−0.78	0.48
37	26 Aug 2006	2057	786	943	PH	164	28 Aug 2006	0425	0.57	0.19	0.32	0.09	736	250	−3.83	1.17
38	12 Sep 2008	1030	91	91	NM	89	14 Sep 2008	0449	0.58	0.10	0.33	0.05	556	96	2.04	0.34
39	29 May 2009	0930	139	139	NM	258	01 Jun 2009	0148	0.56	0.18	0.32	0.09	353	116	0.72	0.32

Column: (1) Event number; (2) – (3) Appearance date [ddmmmyy] and time [hhmm] for an ICME–associated CME observed by SOHO/LASCO; (4) Speed in the sky plane measured by SOHO/LASCO with 0.08 AU of reference distance; (5) Radial speed estimated using $V_{SOHO} = 1.20 \times V_{POS}$; (6) Type of CME [FH, PH, and NM mean Full Halo, Partial Halo, and Normal CME, respectively]; (7) Position angle measured from solar North in degrees (counter-clockwise) [–99 means Full Halo]; (8) – (9) Observation date [ddmmmyy] and mean time [hhmm] for IPS disturbance event day; (10) – (11) Average and standard error for the distance of observed disturbance [R_0]; (12) – (13) Average and standard error for the reference distance [R_1] (in SOHO–IPS region); (14) – (15) Average and standard error for the speed [V_1] (in SOHO–IPS region); (16) – (17) Average and standard error for acceleration [a_1] (in SOHO–IPS region).

Table 2 Properties in the IPS–Earth region derived from IPS observations, detection dates, times, and speeds obtained by *in-situ* observations at 1 AU, fitting parameters and speeds of background solar wind for 39 ICMEs during 1997 – 2009.

	IPS						*in-situ*			Parameters for power-law equation		Transit speed	Background wind	
	IPS–Earth region													
	R_2 [AU]		V_2 [km s^{-1}]		a_2 [m s^{-2}]		Date	Time	V_{Earth}	Index	Coefficient	V_{Tr}	V_{bg} [km s^{-1}]	
No.	Aver.	σ	Aver.	σ	Aver.	σ	[ddmmmyy]	[hhmm]	[km s^{-1}]	α	β	[km s^{-1}]	Aver.	σ
1	0.81	0.07	401	153	–0.35	0.56	10 Dec 1997	1800	350	–0.102	366.9	401	354	24
2	0.75	0.11	809	335	–1.95	2.06	02 May 1998	0500	520	–0.374	547.2	692	369	47
3	0.80	0.05	391	105	–0.20	0.45	07 Nov 1998	2200	450	–0.167	426.9	482	385	27
4	0.78	0.08	399	145	–0.82	0.83	09 Nov 1998	0100	450	–0.478	411.5	544	385	27
5	0.78	0.08	495	165	–0.49	0.73	16 Apr 1999	1800	410	0.094	465.0	480	398	15
6	0.81	0.05	361	101	0.85	0.48	27 Jun 1999	2200	670	–0.340	483.9	516	306	31
7	0.72	0.04	587	80	–0.33	0.47	30 Jul 1999	2000	620	0.111	658.4	654	377	43
8	0.80	0.06	436	112	–0.12	0.49	31 Jul 1999	1900	480	–0.080	466.9	507	545	22
9	0.80	0.07	385	134	–0.32	0.60	20 Aug 1999	2300	460	–0.325	416.8	510	635	67
10	0.75	0.03	630	78	–0.17	0.38	24 May 2000	1200	530	–0.098	530.8	542	579	7
11	0.76	0.09	470	173	0.53	0.60	04 Jun 2000	2200	470	0.022	433.4	378	462	55
12	0.79	0.10	381	177	–0.18	0.71	11 Jul 2000	0200	440	–0.120	423.0	474	371	13
13	0.78	0.09	566	199	–3.46	1.75	13 Jul 2000	1300	610	–0.347	638.2	874	500	24
14	0.80	0.05	816	170	–2.12	1.18	20 Jul 2000	0100	530	–0.079	611.8	648	574	43
15	0.81	0.07	414	149	0.06	0.62	10 Aug 2000	1900	430	0.165	447.8	430	412	36
16	0.77	0.06	793	186	–1.33	1.17	12 Aug 2000	0500	580	–0.090	634.9	686	412	36
17	0.85	0.03	276	59	0.11	0.23	02 Sep 2000	2200	420	–0.398	340.2	417	529	47
18	0.82	0.08	473	218	0.25	1.49	11 Nov 2000	0800	790	–0.492	600.6	730	650	184
19	0.72	0.10	782	253	–2.69	2.28	13 Apr 2001	0900	730	–0.253	753.9	955	537	26
20	0.72	0.04	573	85	–0.27	0.40	17 Aug 2001	2000	500	–0.125	502.2	546	395	43
21	0.82	0.06	722	194	–3.43	1.44	28 Aug 2001	0000	490	–0.441	545.6	752	410	21
22	0.78	0.06	341	100	–1.78	0.92	01 Oct 2001	0800	490	–0.397	467.5	584	513	33
23	0.78	0.10	374	192	0.11	0.64	27 Oct 2001	0300	420	–0.175	379.7	397	393	32
24	0.76	0.04	298	61	–0.39	0.28	29 Oct 2001	2200	360	–0.569	306.2	405	393	32
25	0.75	0.04	477	83	–1.93	0.70	19 Nov 2001	2200	430	–0.553	435.4	644	399	20

Table 2 (Continued)

	IPS						*in-situ*			Parameters for power-law equation		Transit speed	Background wind	
	IPS–Earth region													
	R_2 [AU]		V_2 [km s^{-1}]		a_2 [m s^{-2}]		Date	Time	V_{Earth}	Index	Coefficient	V_{Tr}	V_{bg} [km s^{-1}]	
No.	Aver.	σ	Aver.	σ	Aver.	σ	[ddmmmyy]	[hhmm]	[km s^{-1}]	α	β	[km s^{-1}]	Aver.	σ
26	0.74	0.05	414	81	–0.03	0.34	02 Aug 2002	0600	460	–0.175	424.9	462	428	34
27	0.83	0.10	609	266	–2.42	1.78	08 Sep 2002	0400	470	–0.562	482.9	703	400	22
28	0.76	0.07	858	274	–2.91	2.19	30 May 2003	0200	600	–0.344	649.3	844	662	32
29	0.82	0.05	277	73	–0.89	0.51	17 Jun 2003	1000	480	–0.434	410.4	518	520	44
30	0.84	0.06	666	265	–1.84	1.70	18 Aug 2003	0100	450	0.068	543.0	540	534	55
31	0.81	0.06	460	128	–2.33	0.78	24 Jul 2004	1400	560	–0.220	583.3	762	450	61
32	0.75	0.05	591	114	–0.93	0.66	14 Sep 2004	1500	550	–0.417	516.0	666	286	37
33	0.83	0.08	307	137	–0.38	0.60	30 May 2005	0100	460	–0.254	411.0	507	342	56
34	0.85	0.04	264	65	0.43	0.22	31 May 2005	0400	460	–0.141	370.6	405	342	56
35	0.73	0.06	731	154	–1.93	0.85	10 Jul 2005	1000	430	–0.166	516.8	640	332	11
36	0.85	0.07	300	127	0.09	0.51	09 Aug 2005	0000	480	–0.175	410.9	477	537	82
37	0.78	0.09	283	120	–0.48	0.58	30 Aug 2006	2000	400	–0.429	348.5	437	511	83
38	0.79	0.05	247	58	–0.01	0.20	17 Sep 2008	0400	400	0.486	425.8	366	406	107
39	0.78	0.09	256	103	0.02	0.28	04 Jun 2009	0200	310	0.276	327.7	304	327	26

Column: (1) Event number [identical with column (1) in Table 1]; (2) – (3) Average and standard error for the reference distance [R_2] (in IPS–Earth region); (4) – (5) Average and standard error for the speed [V_2] (in IPS–Earth region); (6) – (7) Average and standard error for the acceleration [a_2] (in IPS–Earth region); (8) – (9) Detection date [ddmmmyy] and time [hhmm] for a near-Earth ICME by *in-situ* observation at 1 AU; (10) Near-Earth ICME speed measured by *in-situ* observation at 1 AU; (11) – (12) Index [α] and coefficient [β] for a power-law form of radial speed evolution; (13) 1 AU transit speed [V_{Tr}] derived from the CME appearance and the ICME detection; (14) – (15) Average and standard deviation for the speed of background wind [V_{bg}] measured by spacecraft including ACE, *Wind*, IMP-8, and *GEOTAIL*.

Table 3 Mean values of coefficients [k_1, k_2, and k_3] for the best-fit quadratic curve $\alpha = k_1 + k_2 V_{SOHO} + k_3 V_{SOHO}^2$ and the critical speed for zero acceleration [V_{c1}], and their standard errors, which were derived from the relationship between V_{SOHO} and α.

	k_1	k_2	k_3	V_{c1} [km s^{-1}]
Mean	4.31×10^{-1}	-1.06×10^{-3}	3.04×10^{-7}	471
Standard error	5.58×10^{-2}	1.16×10^{-4}	5.22×10^{-8}	19

Table 4 Mean values of slope and intercept for the best-fit line and the critical speed for zero acceleration [V_{c2}] and their standard errors, which were derived from the relationship between speeds and accelerations of ICMEs.

	Slope [s^{-1}]	Intercept [m s^{-2}]	V_{c2} [km s^{-1}]
Mean	-7.38×10^{-6}	3.54	480
Standard error	2.03×10^{-7}	1.24×10^{-1}	21

Table 5 Coefficients [γ_1 and γ_2], correlation coefficient [CC], and reduced χ^2 for the linear and quadratic equations

Equation	Mean	Standard error	CC	χ^2
	γ_1 [s^{-1}]			
Linear	6.58×10^{-6}	2.34×10^{-7}	–0.93	1.26
	γ_2 [m^{-1}]			
Quadratic	6.10×10^{-12}	2.25×10^{-13}	–0.90	2.90